
Large Deformation Analysis for Costal Geo-Disasters Using Continuum and Discrete Modeling

A. Yashima, S. Moriguchi, R. Uzuoka, H. Nonoyama,
and K. Sawada

Abstract

Various kinds of geo-disasters have occurred, such as soil avalanches, landslides, failure of river dike, liquefaction and scoring. These disasters have caused serious damage to infrastructures and human activities. Numerical simulations are one of the powerful tools for predicting (1) when the failure will take place, (2) where the failure take place, (3) how far the collapsed soil mass will flow, and (4) how large the impact force to structures will be. In this paper, FEM, CFD, DEM and SPH are introduced as numerical methods for costal geo-disasters. Brief explanation of theory of each numerical method will be described in this paper. Based on simulated results, advantages and disadvantages of different methods are discussed.

Keywords

Geo-disasters • FEM • CFD • DEM • SPH

1 Introduction

A lot of disasters have occurred in the world. Infrastructures and human lives have been damaged by costal geo-disasters. There are various kinds of costal geo-disasters reported as shown in Fig. 1. Researchers and government officers of

each country are making effort to reduce the damage, It is however still difficult to prevent those disasters.

Numerical simulations are one of the powerful tools for predicting geo-disasters (1) when the failure will take place, (2) where the failure take place, (3) how far the collapsed soil mass will flow, and (4) how large the impact force to structures will be. Today, we have many kinds of numerical methods, such as Finite Element Method (FEM), Boundary Element Method (BEM), Computational Fluid Dynamics, Smoothed Particle Hydrodynamics (SPH) (Lucy 1977; Gingold and Monaghan 1977), Discrete Element Method (DEM) (Cudall and Strack 1979) and Discontinues Deformation Analysis (DDA). These methods are roughly categorized based on deformation level (Fig. 2). We can apply a method to simulate costal geo-disasters, but it is necessary to select suitable method based on the deformation level of each geo-disaster. In this paper, typical numerical results by FEM, CFD, DEM and SPH are introduced and advantages and disadvantages of different methods are discussed.

A. Yashima (✉)
Gifu University, 1-1 Yanagido, Gifu, Japan
e-mail: yashima@gifu-u.ac.jp

S. Moriguchi
Department of Civil Engineering, Gifu University,
1-1 Yanagido, Gifu, Japan

R. Uzuoka
Faculty of Engineering, The University of Tokushima, 2-1
Minamijyousanjima-cho, Tokushima, Japan

H. Nonoyama
Department of Civil Engineering, Nagoya University,
Furo-cho, Chikusa-ku, Nagoya, Japan

K. Sawada
River Basin Research Center, Gifu University,
c1-1 Yanagido, Gifu, Japan

Fig. 1 Soil-water interaction related geo-disasters

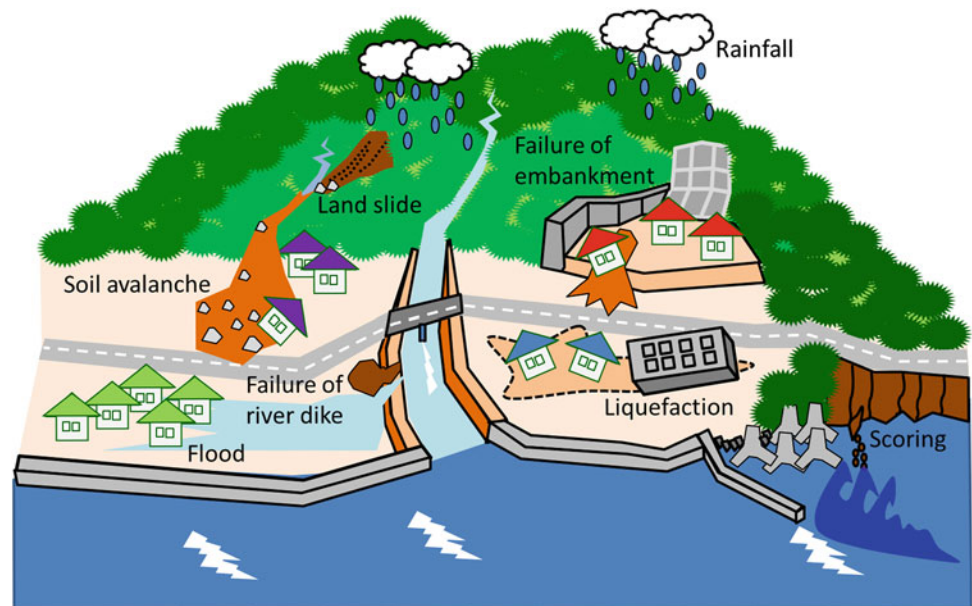
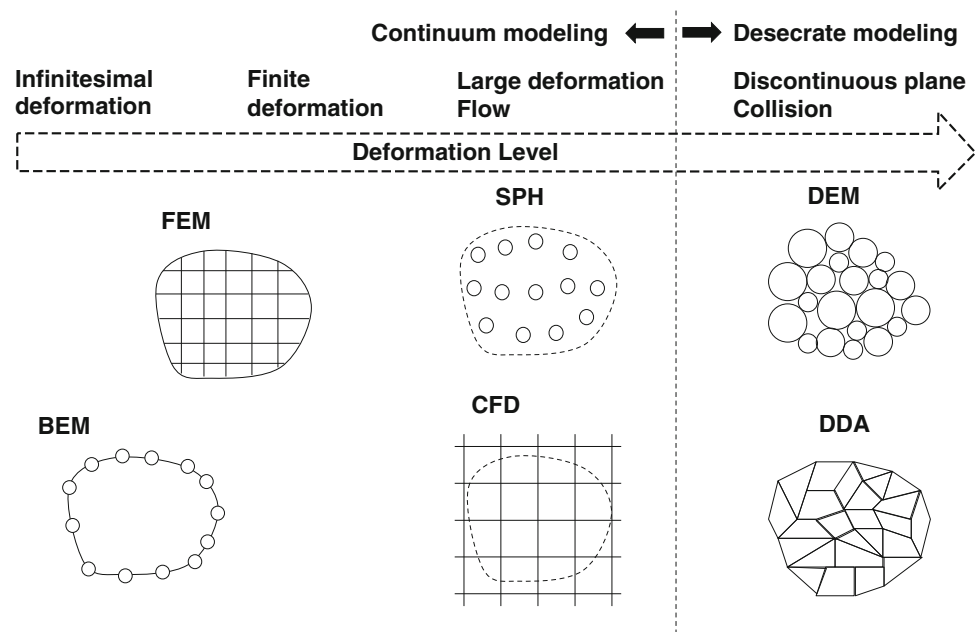


Fig. 2 Numerical methods used in simulations of geo-disasters



2 Stability Analysis Using FEM

A numerical simulation using FEM is introduced in this section. Soil–water coupled FEM analyses based on Biot’s porous media theory (Biot 1962) have been studied since 1970s (e.g. Zienkiewicz and Shiomi 1984), and a lot of important research achievements that are about saturated soils have been reported. However, prediction of behaviours of unsaturated soils are still challenging research topic. In this paper, a dynamic stability analysis of unsaturated slope is shown. The seismic behavior of unsaturated and saturated fill and the failure process are discussed through the numerical simulations. In addition, the

effect of the ground water level on the seismic behavior is discussed through parametric studies.

2.1 Governing Equations

Using porous media theory (de Boer 2000; Schrefler 2002), we derive the governing equations which include the momentum balance equations of the overall three-phase material (soil, water and air) and the mass and momentum balance equations of the pore water and air. The details of the numerical method are referred to Uzuoka and Borja (2011).

Mass balance equation for α phase ($\alpha = (s : \text{soil}, w : \text{water}, a : \text{air})$) is

$$\frac{D^\alpha \rho^\alpha}{Dt} + \rho^\alpha \text{div} \mathbf{v}^\alpha = 0 \quad (1)$$

where D^α/Dt is the material time derivative with respect to α phase, ρ^α is the partial density of α phase, \mathbf{v}^α is the velocity vector of α phase. The mass exchange among three phases is ignored here. The linear momentum balance equation of α phase is

$$\rho^\alpha \frac{D^\alpha \mathbf{v}^\alpha}{Dt} = \rho^\alpha \mathbf{a}^\alpha = \text{div} \boldsymbol{\sigma}^\alpha + \rho^\alpha \mathbf{b} + \hat{\mathbf{p}}^\alpha \quad (2)$$

where \mathbf{a}^α is the acceleration vector of α phase, $\boldsymbol{\sigma}^\alpha$ is the Cauchy stress tensor of α phase, \mathbf{b} is the body force vector, $\hat{\mathbf{p}}^\alpha$ is the interaction vector of α phase between other phases.

Constitutive equations are the followings. The partial Cauchy stress of each phase is derived (e.g. Borja 2006) as

$$\begin{aligned} \boldsymbol{\sigma}^s &= \boldsymbol{\sigma}' - (1-n)(s^w p^w + s^a p^a) \mathbf{I}, \quad \boldsymbol{\sigma}^w = -n s^w p^w \mathbf{I}, \\ \boldsymbol{\sigma}^a &= -n s^a p^a \mathbf{I} \end{aligned} \quad (3)$$

where $\boldsymbol{\sigma}'$ is the effective stress tensor, so-called average skeleton stress (Gallipoli et al. 2003), p^w is the pore water pressure and p^a is the pore air pressure. The stress is defined as positive in tension and the pressures are defined as positive in compression. n is the porosity, s^w is the degree of water saturation, and s^a is the degree of air saturation. The interaction vector for each phase is assumed as

$$\hat{\mathbf{p}}^s = -\hat{\mathbf{p}}^w - \hat{\mathbf{p}}^a, \quad \hat{\mathbf{p}}^\alpha = p^\alpha \text{grad} n^\alpha - \frac{n^\alpha \rho^{\alpha R} g}{k^{\alpha s}} n^\alpha \mathbf{v}^{\alpha s} \quad (4)$$

where g is the gravity acceleration, n^α is the volume fractions of α phase, $\rho^{\alpha R}$ is the intrinsic density of α phase, $k^{\alpha s}$ is the permeability coefficient of α phase (water or air). The compressibility of pore water under an isothermal condition is assumed as

$$\frac{D^s \rho^{wR}}{Dt} = \frac{\rho^{wR}}{K^w} \frac{D^s p^w}{Dt} \quad (5)$$

where K^w is the bulk modulus of pore water. The compressibility of pore air under an isothermal condition assumed as

$$\frac{D^s \rho^{aR}}{Dt} = \frac{1}{\Theta \bar{R}} \frac{D^s p^a}{Dt} \quad (6)$$

where Θ is the absolute temperature and \bar{R} is the specific gas constant of air. The constitutive relation between water saturation and suction is assumed as

$$\frac{D^s s^w}{Dt} = c \frac{D^s p^c}{Dt} = c \frac{D^s (p^a - p^w)}{Dt} \quad (7)$$

where c is the specific water capacity and p^c is the suction. The specific water capacity is calculated from the water retention curve (WRC) as shown in the next section.

Combining the balance and constitutive equations, we derive the governing equations which include the momentum balance equations of the over-all three-phase material and the mass and momentum balance equations of the pore water and air with the following assumptions. (1) the soil particle is incompressible, (2) the mass exchange among phases is neglected, (3) The material time derivative of relative velocities and advection terms of pore fluids to the soil skeleton are neglected, (4) an isothermal condition are assumed. The momentum balance equation of the overall three-phase material is derived as

$$\rho \mathbf{a}^s = \text{div} \{ \boldsymbol{\sigma}' - (s^w p^w + s^a p^a) \mathbf{I} \} + \rho \mathbf{b} \quad (8)$$

where ρ is the overall density of three-phase material and \mathbf{a}^s is the acceleration vector of soil skeleton. The mass and momentum balance equations of the pore water and air are derived as

$$\begin{aligned} n \left(\frac{s^w p^{wR}}{K^w} - \rho^{wR} c \right) \frac{D^s p^w}{Dt} + n \rho^{wR} c \frac{D^s p^a}{Dt} + s^w \rho^{wR} \text{div} \mathbf{v}^s \\ + \text{div} \left\{ \frac{k^{ws}}{g} (-\text{grad} p^w + \rho^{wR} \mathbf{b} - \rho^{wR} \mathbf{a}^s) \right\} = 0 \end{aligned} \quad (9)$$

$$\begin{aligned} n \left(\frac{s^a}{\Theta \bar{R}} - \rho^{aR} c \right) \frac{D^s p^a}{Dt} + n \rho^{aR} c \frac{D^s p^w}{Dt} + s^a \rho^{aR} \text{div} \mathbf{v}^s \\ + \text{div} \left\{ \frac{k^{as}}{g} (-\text{grad} p^a + \rho^{aR} \mathbf{b} - \rho^{aR} \mathbf{a}^s) \right\} = 0 \end{aligned} \quad (10)$$

where ρ^{wR} and ρ^{aR} are the intrinsic densities of pore water and air respectively, \mathbf{v}^s is the velocity vector of soil skeleton, k^{ws} and k^{as} are the permeability coefficient of water and air respectively. This simplified formulation is called u-p^w-p^a formulation. Although the governing equations are derived in the regime of finite strain, we assume infinitesimal strain in the following study for simplicity.

2.2 Constitutive Equations

2.2.1 Constitutive Equation for Water Retention Curve

The specific water capacity c is calculated from the water retention curve (WRC). The WRC is assumed as

$$\begin{aligned} s^w &= (s_s^w - s_r^w) s_e^w + s_r^w, \quad s_e^w = \{1 + \exp(a_{lg} p^c + b_{lg})\}^{-c_{lg}}, \\ p^c &= p^a - p^w \end{aligned} \quad (11)$$

where s_s^w is the saturated (maximum) degree of saturation, s_r^w is the residual (minimum) degree of saturation and s_e^w is the effective water saturation. The relationship between s_e^w and suction p^c is assumed as a logistic function with the material parameters a_{lg} , b_{lg} and c_{lg} . The logistic WRC is a

Fig. 3 Aerial photograph of the collapsed fill slope (Miyagi Engineering Co. Ltd.)



continuous function at $p^c = 0$; therefore the convergence in the iterative numerical scheme can be achieved (Uzuoka and Borja 2011). The above WRC is modified to fit “wetting” curve during undrained cyclic shear as shown in later. The permeability coefficient of water and air are assumed to be dependent on the effective water saturation as

$$k^{ws} = k_s^w (s_e^w)^{\xi_k}, \quad k^{as} = k_s^a (1 - s_e^w)^{\eta_k} \quad (12)$$

where k_s^w is the saturated (maximum) coefficient of water permeability, k_s^a is the dry (maximum) coefficient of air permeability, ξ_k and η_k are the material parameters.

2.2.2 Constitutive Equation for Effective Stress

A simplified elasto-plastic constitutive equation for effective stress is used here. Assuming that plastic deformation occurs only when the deviatoric stress ratio changes, the yield function is assumed as

$$f = \sqrt{\frac{3}{2}} \|\boldsymbol{\eta} - \boldsymbol{\alpha}\| - k = \sqrt{\frac{3}{2}} \|\mathbf{s}/p' - \boldsymbol{\alpha}\| - k = 0 \quad (13)$$

where p' is the mean effective stress, \mathbf{s} is the deviatoric stress tensor, k is the material parameter which defines the elastic region. $\boldsymbol{\alpha}$ is the kinematic hardening parameter (back stress) and its nonlinear evolution rule (Armstrong and Frederick 1966) is assumed as

$$\dot{\boldsymbol{\alpha}} = a \left(\frac{2}{3} b \dot{\mathbf{e}}^p - \boldsymbol{\alpha} \dot{\varepsilon}_d^p \right), \quad \dot{\varepsilon}_d^p = \sqrt{\frac{2}{3}} \|\dot{\mathbf{e}}^p\| \quad (14)$$

where a, b are the material parameters, $\dot{\mathbf{e}}^p$ is the plastic deviatoric strain rate tensor. With non-associated flow rule, the plastic potential function is assumed as

$$g = \sqrt{\frac{3}{2}} \|\boldsymbol{\eta} - \boldsymbol{\alpha}\| + M_m \ln(p'/p'_a) = 0 \quad (15)$$

where M_m is the material parameter which defines the critical state ratio, p'_a is p' when $\|\boldsymbol{\eta} - \boldsymbol{\alpha}\| = 0$. Finally the elastic module are assumed as

$$K^e = -K^* p' \quad G^e = -G^* p' \quad (16)$$

where K^e is the elastic bulk modulus, G^e is the elastic shear modulus, K^* and G^* are the dimensionless elastic module respectively.

2.3 A Real Fill Slope Failure

Failure of an actual fill slope is reproduced using the dynamic three-phase coupled method explained in previous sub sections. The fill slope is located on old valley at Tsukidate town in Miyagi prefecture. Figure 3 shows an aerial photo of the site after the failure. The fill slope in Fig. 4 was partially collapsed and flowed during the 2003 Miyagi earthquake (Uzuoka et al. 2005). The fill material is a volcanic sandy soil.

2.4 Simulations of the Real Fill Slope Failure

The fill slope failure explained in previous subsection is reproduced using two dimensional seismic analysis.

Fig. 4 Damaged fill slope during the 2003 Miyagi earthquake (Uzuoka et al. 2005)

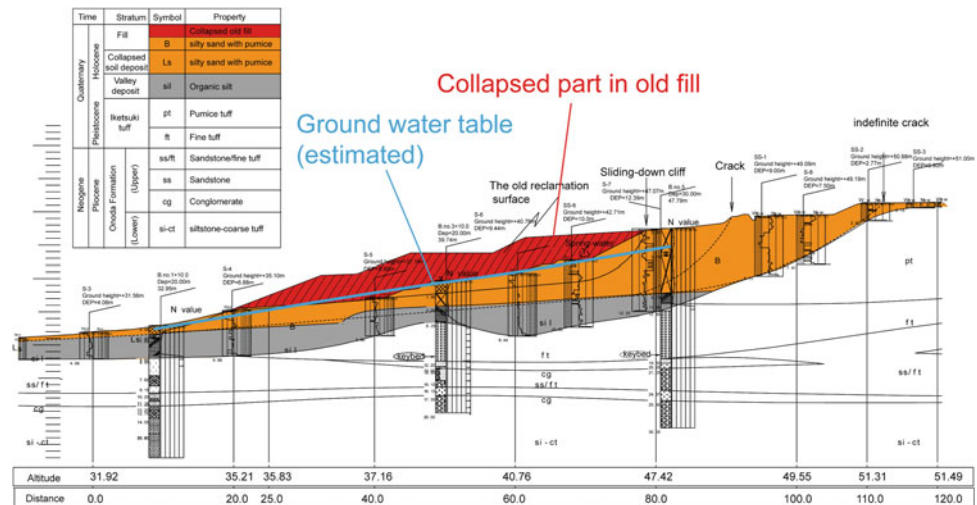
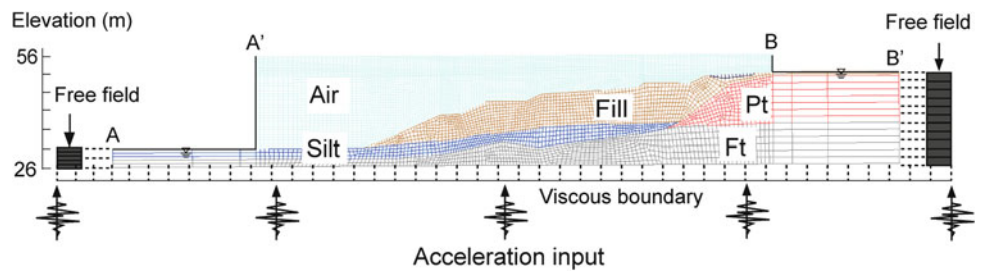


Fig. 5 Two dimensional models and boundary conditions of the fill



Assuming plane strain condition, the cross section is used for finite element modelling. Figure 5 shows a numerical model used in this simulation. The fill is elasto-plastic material, pumice tuff (Pt) and fine tuff (Ft) are linear elastic material with Lamé's constants λ and μ . Kelvin type viscosity is assumed in all materials and its viscous coefficient is proportional to the elastic modulus with a multiplier coefficient α . Table 1 shows the material parameters for each layer. Other parameters of fill material (elasto-plastic material) are summarized in Table 2. The material parameters of the constitutive models for effective stress and WRC are determined through the calibration of the undrained cyclic triaxial tests with unsaturated soil (Kazama et al. 2006).

In the seismic analysis, the input acceleration in Fig. 6 is applied through dampers at the bottom. The lateral boundaries are also supported with dampers which are connected to the free field motions. The free field motions are separately calculated by one dimensional seismic response analyses. The input acceleration history is a calculated wave by using empirical Green's function method using two aftershocks comparing several seismic intensities surrounding Tsukidate town (Fukumoto et al. 2007).

Before the seismic analysis, a static self-weight analysis is performed in order to determine the initial stress and moisture conditions. The soil displacement at the bottom boundary is fixed in all directions and the side boundaries are vertical rollers. The bottom and right boundaries are impermeable. A–

A' and B–B' lines in Fig. 5 are permeable with constant total water heads. These water heads are assumed to reproduce the ground water levels as estimated in Fig. 4. The ground water level was estimated to be low because it had not rained for a week before the earthquake. However the actual ground water level was not measured before the earthquake. Mori et al. (2011) showed that the ground water level in a fill slope significantly affected the seismic behavior of fill slope; therefore we perform parametric studies in order to discuss the effect of the ground water level on the seismic behavior of fill slope. In additional case, continuous rain of 1 mm/day for 10 days is considered to simulate high ground water level in the fill slope. Thus two different situations of water level are considered, the case of low water level (Case 1) and the case of high water level (Case 2).

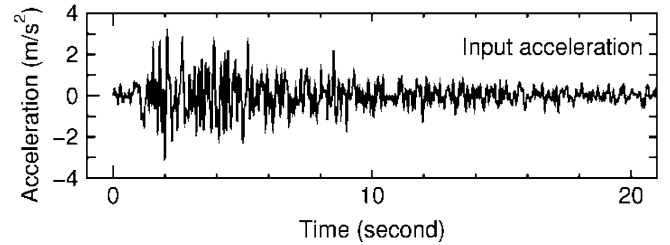
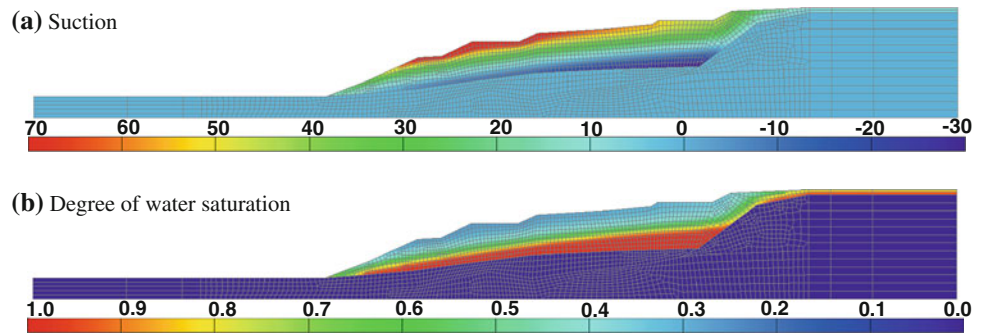
Figure 7 shows the initial distributions of suction and water saturation in the elasto-plastic fill obtained by the static self-weight analysis in Case 1. The air entry value of the fill is about 10 kPa, therefore the boundary between saturated and unsaturated portions is located slightly above the ground water table. The ground water table roughly agrees with the measured one after the earthquake (Uzuoka et al. 2005). Figure 8 shows results of Case 1, the distributions of absolute horizontal displacement, deviatoric strain and effective stress reduction ratio (ESRR) after the earthquake. The ESRR is defined as $1 - p'/p'_0$ where p'_0 is the initial value of mean effective stress. Large deviatoric strain is generated around the toe and top of

Table 1 Material parameters for all soil layers

	Fill	Silt	Pt	Ft
Porosity, n	0.48	0.43	0.43	0.43
Intrinsic density of soil skeleton, $\rho^{sR}(\text{t/m}^3)$	2.48	2.68	2.74	2.74
Intrinsic density of water, $\rho^{wR}(\text{t/m}^3)$	1.0	1.0	1.0	1.0
Permeability coefficient of water, $k_s^w(\text{m/s})$	1.1×10^{-4}	1.0×10^{-9}	1.0×10^{-11}	1.0×10^{-11}
Permeability coefficient of air, $k_s^a(\text{m/s})$	1.0×10^{-6}	1.0×10^{-10}	1.0×10^{-12}	1.0×10^{-12}
Permeability parameters of water and air, ξ_k/η_k	3.0/0.33			
Lame's constant, λ (kPa)		181812	437290	1125000
Lame's constant, μ (kPa)		45453	437290	1125000
Viscous coefficient parameter, α	0.001	0.0048	0.0019	0.00096

Table 2 Material parameters of the fill

Elasto-plastic model parameters		WRC parameters	
Dimensionless shear modulus, G^*	600	Maximum degree of saturation, s_s^w	0.99
Dimensionless bulk modulus, K^*	30	Minimum degree of saturation, s_t^w	0.255
Nonlinear hardening parameter, a	857	Main drying curve, a_{lg}, b_{lg}, c_{lg}	7, 7, 0.05
Nonlinear hardening parameter, b	-1.47	Main wetting curve, a_{lg}, b_{lg}, c_{lg}	0.037, 1, -2
Critical state stress ratio, M_m	1.47	Scaling parameter, p_2^c (kPa)	-5
Yield function parameter, k	0.09		
Physical parameters			
Porosity, n	0.48	Intrinsic density of air, ρ^R (t/m^3)	1.23×10^{-3}
Bulk modulus of water, K^w (kPa)	2.0×10^6	Gas parameter, $1/\bar{R}\bar{\theta}$ (s^2/m^2)	1.25×10^{-5}

Fig. 6 Time history of input acceleration (Fukumoto et al. 2007)**Fig. 7** Initial distributions of suction and water saturation before the earthquake (Case 1). **a** Suction, **b** Degree of water saturation

the fill near the base. Corresponding to the strain distribution, residual horizontal displacement around the toe and top of the fill is large leftward, which is comparable to the damaged configuration of the fill in Fig. 4. The ESRR in the fill does not

reach 1.0. Therefore complete liquefaction does not occur even in the saturated part. However, the ESRR in the unsaturated fill above the ground water table reaches about 0.8, which reduces the stiffness and strength of unsaturated fill.

Fig. 8 Distributions of displacement, deviatoric strain and ESRR after the earthquake (Case 1). **a** Absolute horizontal displacement, **b** Deviatoric strain, **c** Effective stress reduction ratio (ESRR)

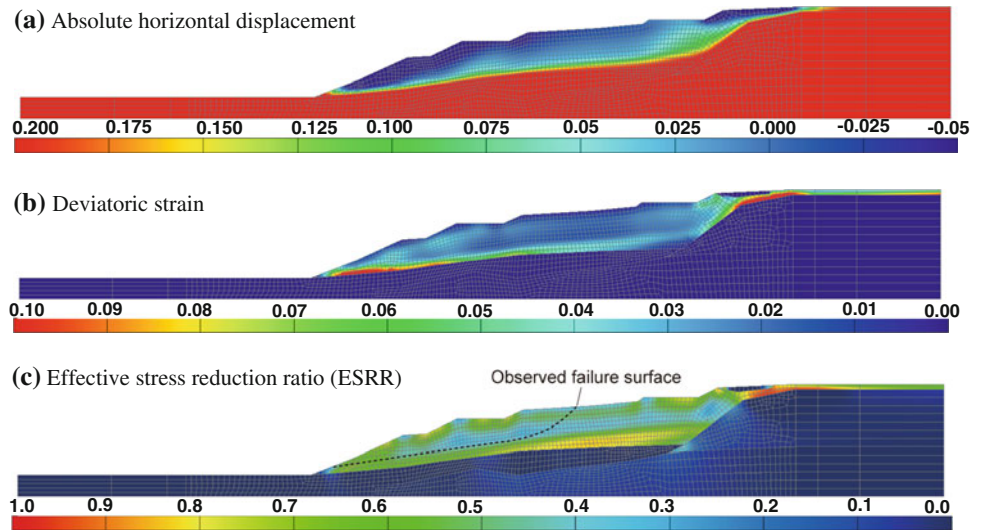


Fig. 9 Distributions of suction and water saturation before the earthquake (Case 2). **a** Suction, **b** Degree of water saturation

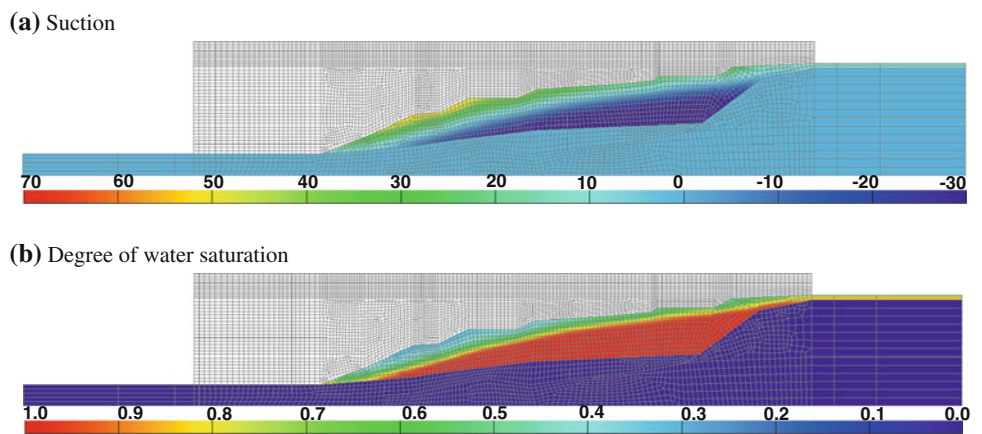


Figure 9 shows the initial distributions of suction and water saturation in Case 2 (high water level condition). Figure 10 shows the distributions of absolute horizontal displacement, deviatoric strain and effective stress reduction ratio (ESRR) obtained in Case 2. Large deviatoric strain is generated around the toe and top of the fill near the base similar to the previous case in Fig. 8. In addition, larger deviatoric strain is generated along the ground water level in the middle part. Corresponding to the strain distribution, residual horizontal displacement of the whole fill slope is large leftward, which is not comparable to the damaged configuration of the fill in Fig. 4. The ESRR in the fill reaches about 0.9 near the top of the slope in the saturated part. Therefore complete liquefaction does not occur even with high ground water level. The deformation mode in Case 2 does not correspond to the observed one. Thus real ground water level is estimated to be lower than that in Case 2. It can be therefore summarized water level assumed in Case 1 corresponds to real water level.

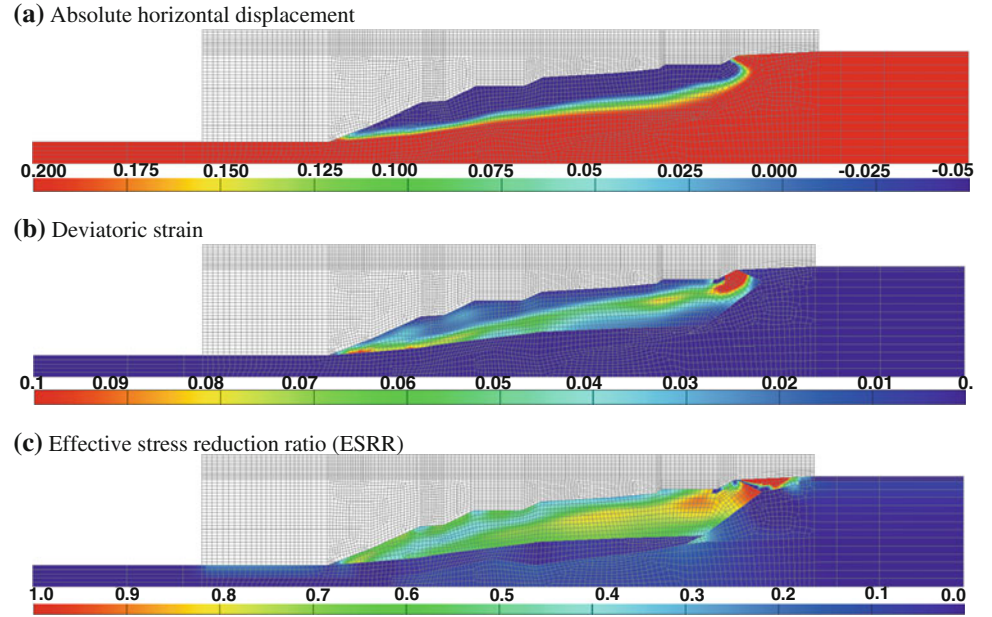
2.5 Sammy of FEM

As shown in this section, FEM can predict behaviors of saturated and unsaturated grounds under seismic condition. By using developed numerical framework and constitutive models, we can predict various kinds of behaviors of soils. In addition, FEM is well known in engineering field, and it has high reliability. These are advantages of FEM. There is however a disadvantage. When FEM is applied to large deformation problems, it is difficult to keep enough calculation accuracy due to mesh distortion.

3 Flow Simulation Using CFD and DEM

Some results of flow simulations of soils using CFD and DEM are introduced in this section. First, numerical framework of CFD based method is explained, and then a flow simulation of the real fill slope explained in previous section is shown. Second, numerical framework of DEM is

Fig. 10 Distributions of displacement, deviatoric strain and ESRR after the earthquake (Case 2). **a** Absolute horizontal displacement, **b** Deviatoric strain **c** Effective stress reduction ratio (ESRR)



shown briefly. Then simulations of sand flow simulation using both CFD and DEM are introduced.

3.1 Numerical Framework of CFD Based Method

An Eulerian type CFD based method is proposed for flow problems of soils, such as soil avalanche, high speed landslide, sediment flow after slope failure (e.g. Moriguchi et al. 2005, 2009; Sawada et al. 2004). In the method, soils are assumed to be Bingham fluid which is one of the non-Newtonian fluids. Bingham fluid model is described by following equation in one dimensional condition.

$$\tau = \eta_0 \dot{\gamma} + \tau_{\min} \quad (17)$$

where τ is the shear stress, η_0 is the viscosity after yield, $\dot{\gamma}$ is the shear strain rate and τ_{\min} the yield strength. When shear stresses below the yield stress, a Bingham fluid behaves as a rigid body and does not deform, but when the shear stress surpasses the yield stress, flow failure occurs resulting in very large deformations. The following Coulomb equation is widely accepted to express the shear strength of a given soil.

$$s = c + \sigma \tan \varphi \quad (18)$$

where s is the shear strength, c is the cohesion, σ is the normal stress and φ is the internal friction angle. In this study, we use this basic failure criterion to formulate a constitutive model for geometricals subjected to flow. Substituting the shear strength s in Eq. (18) by the yield strength τ_{\min} in Eq. (17) and representing the normal stress σ by the hydraulic pressure p , following modified Bingham model is obtained.

$$\tau = \eta' \dot{\gamma} + c + p \tan \varphi \quad (19)$$

By formulating above equation, we can obtain an equivalent Newtonian viscosity of Bingham fluid as follows,

$$\eta' = \frac{\tau}{\dot{\gamma}} = \eta_0 + \frac{c + p \tan \varphi}{\dot{\gamma}} \quad (20)$$

The equivalent Newtonian viscosity η' described in above equation is used in governing equation.

In some paper published by authors (Moriguchi et al. 2005; Sawada et al. 2004), soils are treated as compressible material, however, soils are treated as incompressible material in this paper. Detailed numerical formulations are summarized by Moriguchi et al. (2009).

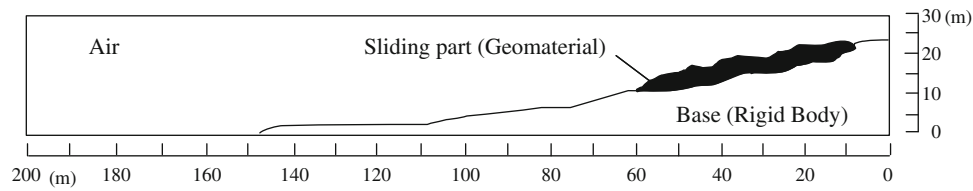
A motion equation of flowing material is represented by the following equation,

$$\frac{\partial \mathbf{u}}{\partial t} + \mathbf{u} \cdot \nabla \mathbf{u} = -\frac{1}{\rho} \nabla p + \frac{2}{\rho} \nabla [\eta'(\mathbf{V})] + \mathbf{g} \quad (21)$$

where, \mathbf{u} is the velocity vector, ρ is the density, \mathbf{V} is the strain rate tensor, \mathbf{g} is the gravity vector. The Confined Interpolation Profile (CIP, Yabe and Aoki 1995) method is used to solve the advection terms of the above equation and other terms are solved using the finite different method. In order to capture the surface of flowing material, an implicit function, called density function, which indicates the occupancy of the material at each calculation point, is used. The change of the density function is solved using Tangent of Hyperbola for Interface Capturing (THINC) method (Xiao et al. 2005). By using the THINC method, we can keep sharp interface even in Eulerian mesh system. In addition, total mass of flow material can be kept.

Table 3 Numerical parameters of flow simulation of the real fill slope failure

	Air	Granular material
ρ Density (kg/m ³)	1.25	1800.0
C_s Sound speed (m/s)	340.0	1500.0
η Viscosity coefficient (Pa · s)	0.00002	–
η_0 Viscosity after yield (Pa · s)		1.0
c Cohesion (Pa)		1000.0
ϕ Internal friction angle (degree)	–	5.7
$\Delta x, \Delta y$ Mesh size (m)	$\Delta x = 2.0 \Delta y = 0.5$	
$N_x \times N_y$ Number of meshes	100 × 60	
g Gravity acceleration (m/s ²)	9.81	

**Fig. 11** Numerical model of flow simulation of the real fill slope failure

3.2 Flow Simulation of the Real Fill Slope Failure

A flow simulation using the CFD based method is introduced in this subsection. The fill slope failure explained in Sect. 2 is targeted also in this simulation. Although process before failure is reproduced in FEM analysis, flow behavior after failure is targeted in this simulation.

In order to determine numerical parameters, sample soil is obtained in the site of fill slope failure soon after the incident, and some in-site experiments were conducted. In the experiments, a soil-slump test was also carried out. The cohesion and the internal friction angle are determined by conducting a series simulation of soil-slump test (Moriguchi et al. 2005). Numerical parameters determined from the experimental results and the simulated results are shown in Table 3.

From topographic surveying data and related maps, a two-dimensional numerical model was prepared as shown in Fig. 11. The shadow part denotes the sliding part, and non-sliding part in the incident is considered as rigid body in the simulation. The non-slip boundary condition is used for the bottom boundary and surface of the rigid body.

Figure 12 shows simulated surface configurations at different times. As shown in the result, final run-out distance is about 190 m. According to literatures (e.g. Koyanagi 2003; The Japanese Geotechnical Society 2003), observed run-out distance was about 180 m, therefore simulated result corresponds to observed travel distance with high accuracy.

3.3 Brief Explanation of DEM

Because DEM is very famous numerical method, its theory is explained briefly. The method is based on discrete modeling, and its theory is totally different from the other methods introduced in this paper. The method can calculate the movement of assembly of particles and it has been widely used to simulate the behavior of granular material. Generally, an interparticle force model is shown in Fig. 13. Spring and dashpot are considered in both normal and tangential directions and the slider is used to describe the friction angle at the surface of particles. Based on the interparticle force model, collision force is calculated when collision of particles arise, then movement of each particle are calculated. Because of rapid development of performance of computers, large number of particle is getting to be used in recent studies. In addition, not only sphere element but also non-spherical elements is getting to be used for simulation of granular materials.

3.4 A Flow Simulation of a Flume Experiment

3D numerical simulations of sand flow in a small-scale flume experiment are carried out (Denlinger and Iverson 2001) using the DEM (discrete modeling) and the CFD (continuum modeling). The experiment employed a rectangular flume with a bed surface inclined at 31.4 degrees tapering to a horizontal run-out position (shown in Fig. 14). Figure 15 shows the

Fig. 12 Simulated surface configurations

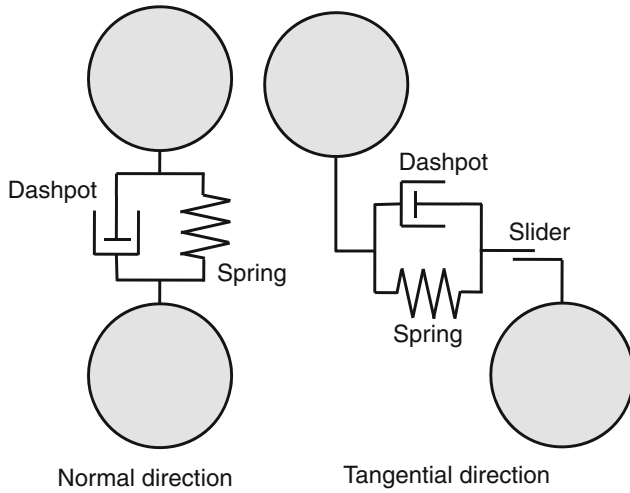
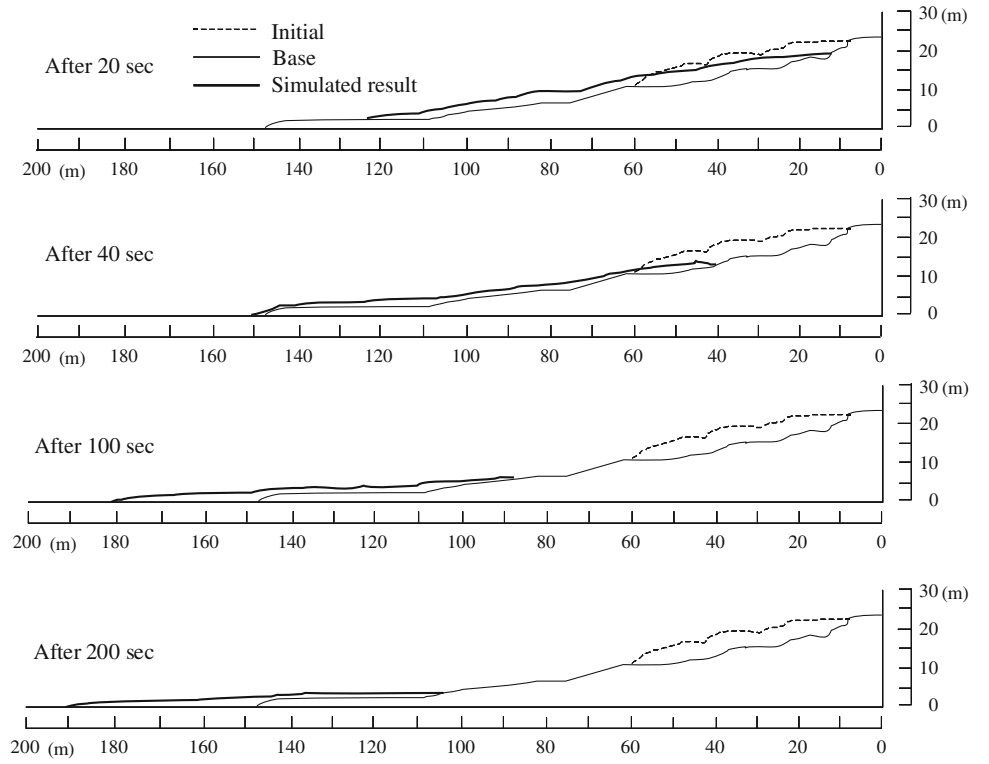


Fig. 13 Interparticle force model of DEM

thickness distribution at different time obtained from the experiment. The internal friction angle and initial density of the sand were 40 degrees and 1600 kg/m^3 . Density of sand grain is 2650 kg/m^3 and typical grain diameter was 0.5 mm.

Figures 16 and 17 show numerical models used in DEM and CFD simulation, respectively. In the DEM simulation, 35,410 spherical particles with diameter 2 mm are set on the top part of the flume considering the initial density of the sand. In the numerical model of CFD simulation, the inclination of the flume is described by changing direction

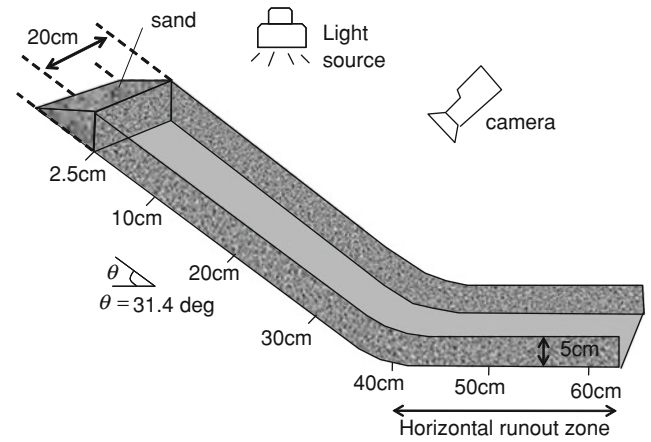


Fig. 14 Model slope used in the experiment

of the gravity acceleration. Parameters used in this simulation are summarized in Table 4. Three cases are considered in both DEM and CFD simulations. In the DEM simulation, the spring coefficient and the dumping coefficient of interparticle model are changed. Same values of the coefficients are used in both normal and tangential direction. 29 degrees is used as the bottom friction angle in all cases. The value is reported in the literature as the static friction angle between sand grain and bottom surface of flume. On the other hand, in CFD simulation, only bottom friction is changed. 29, 20, 15 degrees were used for each cases. Numerical formulation about the bottom friction is

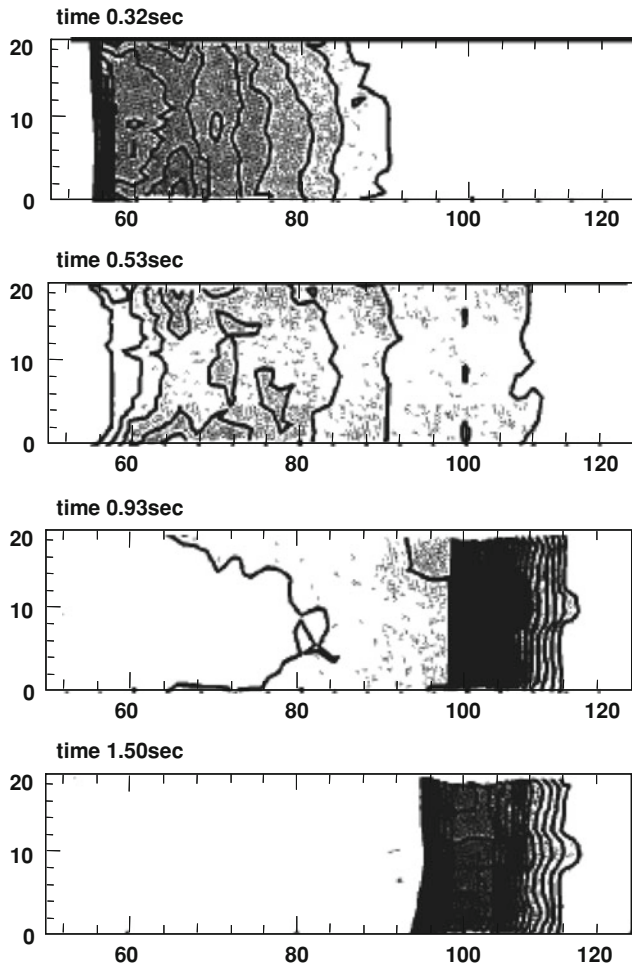


Fig. 15 Thickness distribution of sand (Denlinger and Iverson 2001)

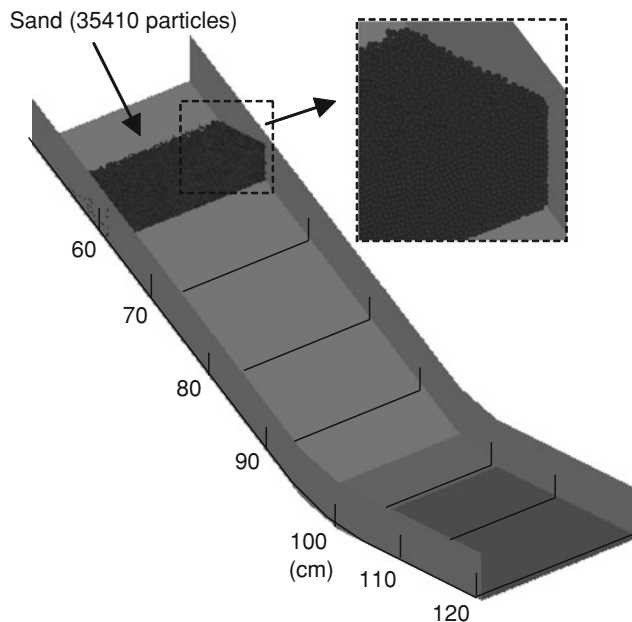


Fig. 16 Numerical model (DEM)

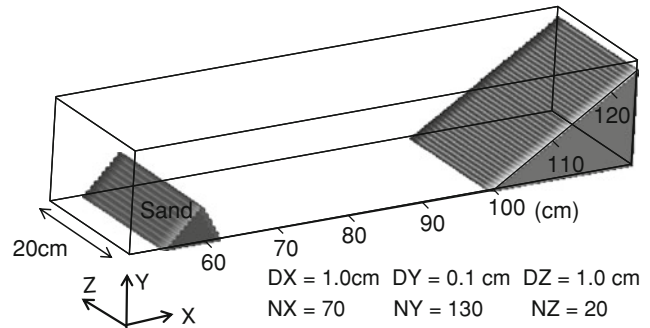


Fig. 17 Numerical model (CFD)

summarized by Moriguchi et al. (2010). Other parameters are determined based on condition of the experiment and are fixed in all cases.

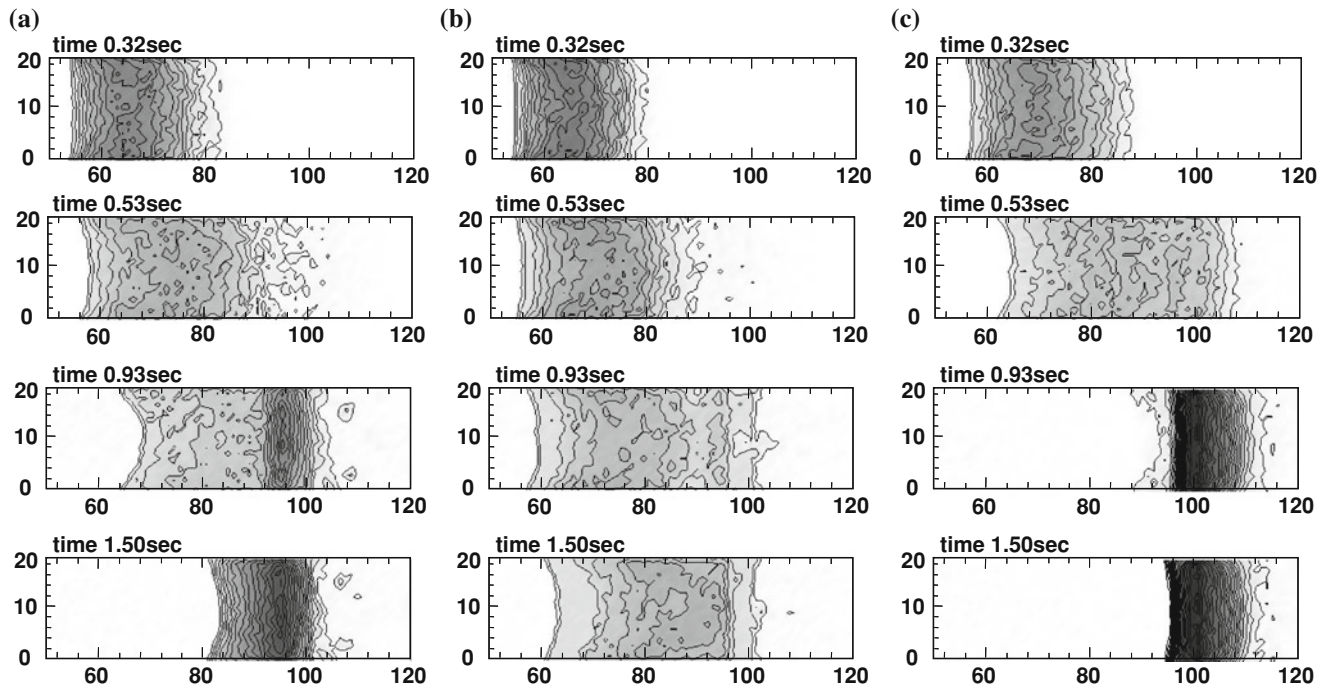
Figures 18 and 19 shows the thickness distributions at different time simulated in DEM and CFD simulations, respectively. As shown in Fig. 18, values of the elastic and the dumping coefficients strongly affect the flow behavior. When the high value of elastic coefficient is used, high fluidity can be seen in the simulated result. In contrast, high value of dumping coefficient makes the flow slower. By adjusting these parameters, it is possible to reproduce the experimental result. The result of Case DEM-3 is in good agreement with the thickness distribution obtained from the experimental. According to the results of CFD simulations (shown in Fig. 19), the simulated flows are strongly depends on the value of the bottom friction, and it is confirmed that the result is in agreement with the experimental result when a small bottom friction angle is used. When 29 degrees are used as bottom friction, the sand dose not reach the end part of the flume and stops on the inclined part. This tendency is totally deferent from the results of the DEM simulation. It can be considered that the different between the DEM and the CFD simulations attribute to the rotation of sand grains. In DEM simulation, the effect of the rotation can be described directly and dynamic friction angle at the bottom surface become lower than 29 degrees. On the other hand, the rotation cannot be considered in the CFD simulation because the method is based on continuum modeling. Therefore we have to use the dynamic friction angle as an input parameter of the bottom friction angle.

3.5 Sammy of CFD and DEM

It is possible to predict flow behaviors of soils by using CFD and DEM. These methods are getting to become strong tool for large deformation problems. However, these methods also have disadvantages. In CFD simulation, it is difficult to keep historical information of soils, such as history of the strain and loading. Thus there is a difficulty when

Table 4 Parameters used in simulations of the flume experiment

Case	Initial density of sand mass (kg/m ³)	Density of sand grain (kg/m ³)	Friction angle of sand (degree)	Bottom friction (degree)	Spring constant (N/m)	Damping coefficient (N s)
DEM-1	1.6X10 ³	2.65 X10 ³	40	29	1.0X 10 ⁶	1.0X 10 ⁶
DEM-2	1.6X10 ³	2.65 X10 ³	40	29	1.0X 10 ⁶	5.0X 10 ³
DEM-3	1.6X10 ³	2.65 X10 ³	40	29	5.0X 10 ⁶	3.0X 10 ³
CFD-1	1.6X10 ³	–	40	29	–	–
CFD-2	1.6X10 ³	–	40	20	–	–
CFD-3	1.6X 10 ³	–	40	15	–	–

**Fig. 18** Thickness distributions of sand (DEM). **a** DEM-1, **b** DEM-2, **c** DEM-3

constitutive models developed in the research field of geomechanics are used in the simulation. It is important to select problems with engineering judgment. Disadvantage of DEM is difficulty of parameter setting. Although some research achievements have been reported, problem of parameter setting is not solved completely.

4 Continuous Simulations of Deformation, Failure and Flow Using SPH

An example of SPH method is introduced in this section. As explained in previous sections, FEM, CFD and DEM have each applicable scope that depends on deformation level. In contrast, applicable scope of SPH is not restricted by

deformation level. In other word, SPH can simulate all deformation level, such as small deformation, failure and flow. In this section, basic theory of SPH is explained, and then a simulation of real scale excavation experiment is shown. Numerical results of SPH are compared with experimental results, results of FEM, the safety factor obtained from conventional limit equilibrium method. Based on the comparison, advantages and disadvantages of SPH are discussed.

4.1 Basic Theory of SPH

SPH method is one of the particle methods. In the method, objects are expressed as an assembly of particles. If the motions of the particles are solved individually, the

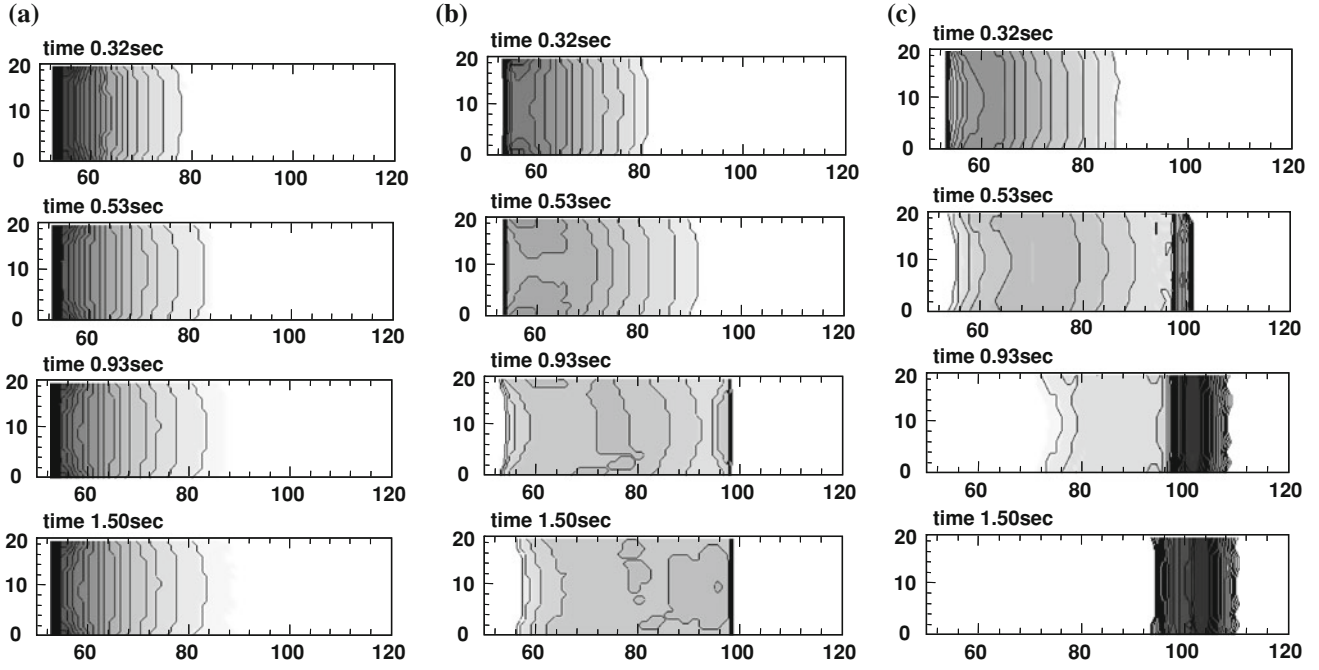


Fig. 19 Thickness distributions of sand (CFD). **a** CFD-1, **b** CFD-2, **c** CFD-3

deformation behavior of the continuum cannot be represented by this technique. In order to treat an object as a continuum, a unique interpolation theory is used. This interpolation theory includes two key approximations: a kernel approximation and a particle approximation. Using the kernel approximation, a bell-shaped distribution profile is estimated around a reference particle α .

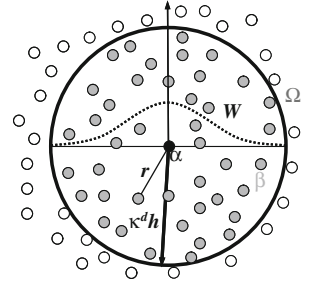
The kernel approximations are based on neighboring particles β located at points x^β within the support domain $\kappa^d h$ of a smoothing function W for the reference particle α , which is located at point x^α , as shown in Fig. 20.

Here, κ^d is a parameter that determines the radius of the support domain and is determined by the smoothing functions. Also, h is the radius of the influence domain. The radius of the support domain is obtained by multiplying the radius of the influence domain by the parameter κ^d . The radius of the influence domain is obtained by multiplying the initial interparticle distance by the parameter β^h . In the first step of the interpolation, we define a smoothed physical quantity $\langle f(x^\alpha) \rangle$ for the physical quantity $f(x^\alpha)$ at the reference particle α as follows:

$$\langle f(x^\alpha) \rangle = \int_{\Omega} f(x^\beta) W(x^\alpha - x^\beta, h) dx = \int_{\Omega} f(x^\beta) W(r, h) dx^\beta \quad (22)$$

where $r = |x^\alpha - x^\beta|$ and Ω is the volume of the integral that contains x^α and x^β . The smoothing function W satisfies the following three conditions.

Fig. 20 Expression of a physical quantity using the SPH method



The first condition is the normalization condition:

$$\int_{\Omega} W(r, h) dx^\beta = 1 \quad (23)$$

The second condition is the delta function property, which holds when the smoothing length approaches zero:

$$\lim_{h \rightarrow 0} W(r, h) = \delta(r) \quad (24)$$

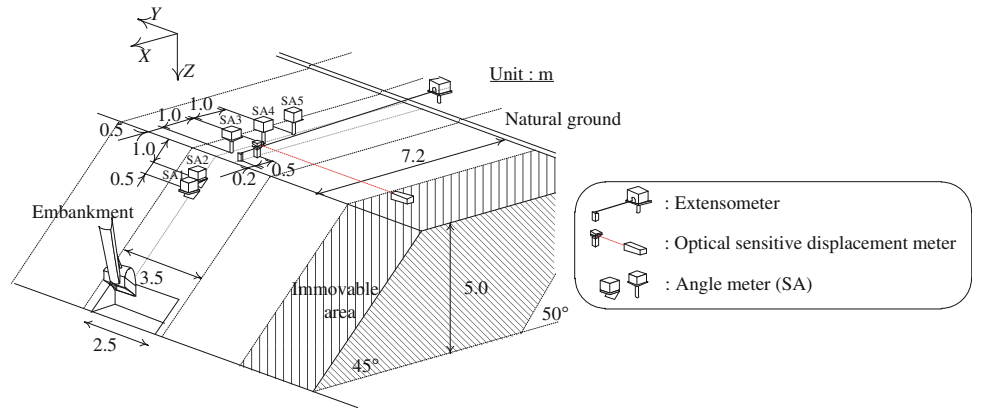
The third condition is the compactness condition:

$$\lim_{h \rightarrow 0} W(r, h) = 0 \quad \text{when } |x^\alpha - x^\beta| > \kappa^d h \quad (25)$$

where defines the nonzero area of the smoothing function.

In the second step of the interpolation, the physical quantity $\langle f(x^\alpha) \rangle$ for the reference particle α is expressed as the summation of the distribution of the assumed physical quantities $f(x^\beta)$ for each particle. Thus, the physical quantity can be expressed in terms of N discrete points:

Fig. 21 Schematic view of the field test setup (Itoh and Toyosawa 2009)



$$dx^\beta = \frac{m^\beta}{\rho^\beta} \quad (26)$$

where dx^β is the volume, m^β is the mass, and ρ^β is the density of the neighboring particles β . Equation (22) is transformed via the above equation as follows:

$$\langle f(x^\alpha) \rangle = \sum_{\beta}^N \frac{m^\beta}{\rho^\beta} f(x^\beta) W(r, h) = \sum_{\beta}^N \frac{m^\beta}{\rho^\beta} f(x^\beta) W^{\alpha\beta} \quad (27)$$

where $W^{\alpha\beta}$ is the smoothing function that expresses the contribution from the neighboring particles β to the reference particle α . Equation (27) is a formula for evaluating a physical quantity via the SPH method. It is also possible to approximate the spatial gradient of a physical quantity in a similar way, using the spatial derivative of the smoothing function. The spatial derivative of Eq. (22) can be written as

$$\begin{aligned} \nabla \langle f(x^\alpha) \rangle &= \nabla \int_{\Omega} f(x^\beta) W(x^\alpha - x^\beta, h) dx^\beta \\ &= \int_{\Omega} f(x^\beta) \nabla W(r, h) dx^\beta \\ &= \int_{\Omega} f(x^\beta) \nabla W^{\alpha\beta} dx^\beta = \sum_{\beta}^N \frac{m^\beta}{\rho^\beta} f(x^\beta) \nabla W^{\alpha\beta} \end{aligned} \quad (28)$$

Furthermore, the above equation can be transformed as follows:

$$\nabla \langle f(x^\alpha) \rangle = \frac{1}{\rho^\alpha} \sum_{\beta}^N m^\beta (f(x^\beta) - f(x^\alpha)) \nabla W^{\alpha\beta} \quad (29)$$

$$\nabla \langle f(x^\alpha) \rangle = \rho^\alpha \sum_{\beta}^N m^\beta \left(\frac{f(x^\alpha)}{(\rho^\alpha)^2} + \frac{f(x^\beta)}{(\rho^\beta)^2} \right) \nabla W^{\alpha\beta} \quad (30)$$

where ρ^α is the density of the reference particle α . In the two-step interpolation theory, it is possible to calculate any physical quantity and its first derivative.

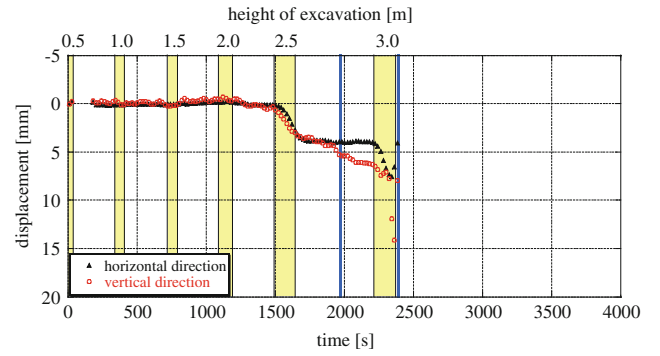


Fig. 22 Time history of the displacement obtained by the optical sensitive displacement meter (Itoh et al. 2007)

4.2 A Real Scale Excavation Experiment

Itoh et al. (2007) conducted a real scale excavation experiment of embankment. The test embankment used in the experiment was 5 m in height and 3.5 m in width, with a slope angle of 45 degrees, and was composed of Kanto Loam and Narita sand. In the experiment, embankments with and without surface compaction were constructed. The failure of the test embankment was triggered by destabilization of the slope due to excavation at the toe of the slope. The slope was excavated using a backhoe, and the excavation was carried out in several stages. The excavation depth for a single stage was about 0.5 m, and the width of the excavation was 2.5 m. After each excavation stage, the slope was left undisturbed for 5 min. Excavation continued until slope failure occurred. Figure 21 shows the positions of the measuring instruments. As shown in the figure, two angle meters were placed on the slope surface, and three angle meters were placed at the top of the slope. An extensometer and an optical sensitive displacement meter were also placed at the top of the slope.

Figure 22 shows the time history of the displacement, obtained in the experiment by the optical sensitive displacement meter placed 0.7 m from the top of slope. Figure 23 shows photos taken at excavation height of 2.5 and 3.0 m. When the excavation depth reached 2.5 m, a 3 mm

Fig. 23 Failure process (Itoh and Toyosawa 2009). **a** at excavation height of 2.5 m, **b** at excavation height of 3.0 m

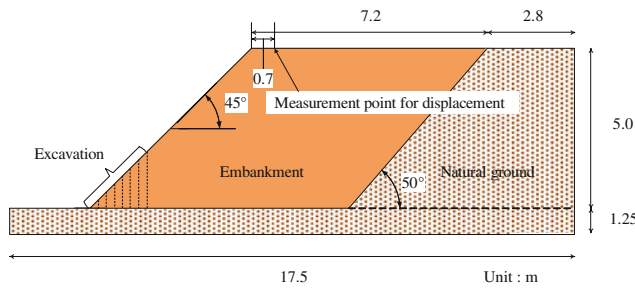


Fig. 24 Numerical model (Koitabashi et al. 2008)

displacement appeared in both the horizontal and vertical directions, and this displacement was maintained in both directions at the conclusion of the stage. A localized slope failure then appeared, as shown in Fig. 23a. Moreover, when the excavation depth reached 3.0 m, a massive failure (including the crown) occurred, as shown in Fig. 23b.

4.3 Simulations of the Real Failure Experiment

The real-scale experiment was reproduced in a previous study, using two- and three-dimensional FEM analyses. Figure 24 illustrates the numerical model used in the FEM analysis. In order to reproduce the conditions of the experiment, the excavation depth for a single stage was set at 0.5 m. In the three-dimensional analysis, the width of the excavation was 2.5 m, and the unexcavated part was simulated. The parameters used in this analysis were determined from in situ laboratory test. In this study, SPH method is applied to simulation of the real-scale

Table 5 Analytical parameters

Number of particles including the wall		10633
Initial interparticle distance	r_0 [m]	0.1
Radius of the support domain	$k^d h$ [m]	0.21
Time increment	Δt [s]	0.0001
Artificial viscosity parameter	$\alpha^{vis}, \beta^{vis}$	1.0
Artificial stress parameter	ϵ^{AS}	0.30

Table 6 Material parameters

		Embankment	Natural ground
Density	γt [kN/m ³]	16.4	20.0
Young's modulus	E [kPa]	4850.0	8000.0
Poisson's ratio	ν	0.35	
Cohesion	c [kPa]	7.68	70.0
Internal friction angle	ϕ [deg]	36.34	5.0
Dilatancy angle	Ψ [deg]	0.0	

experiment. The parameters used in this analysis are listed in Tables 5 and 6. The Drucker–Prager model with a non-associated flow rule is used as the constitutive model. The dilatancy angle was set to 0.0 degree. The isotropic stress corresponding to static earth pressure is used as the initial stress condition. As same as FEM analysis, the excavation is represented by particle (element) removal. For the boundary conditions, the horizontal direction on the side of the natural ground is fixed, and the

Fig. 25 Distribution of maximum shear strain at the different excavation heights.
a Excavation height of 0.5 m,
b Excavation height of 1.0 m,
c Excavation height of 1.5 m,
d Excavation height of 2.0 m,
e Excavation depth of 2.5 m

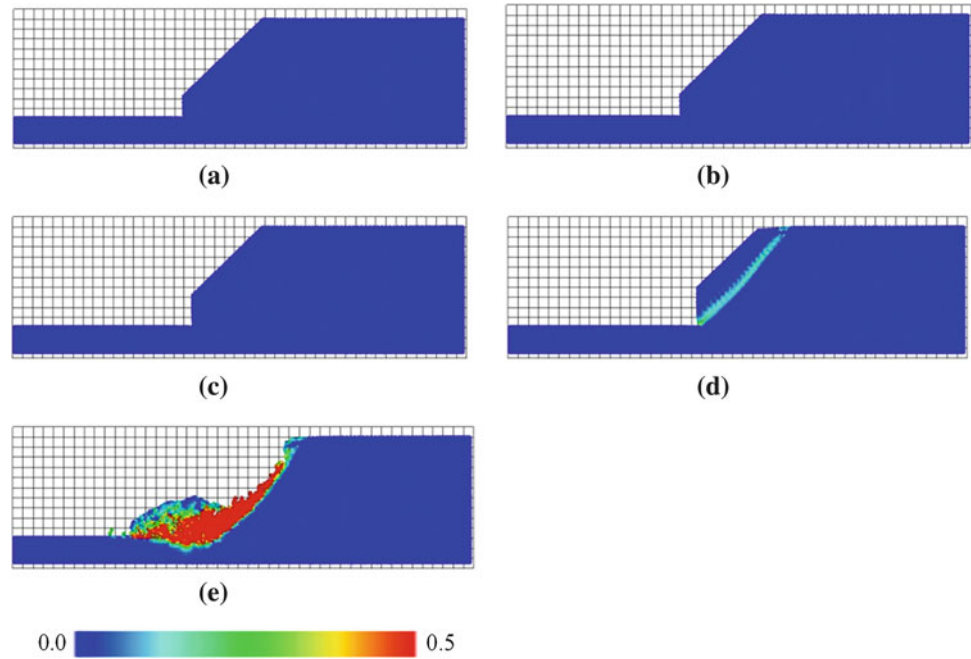
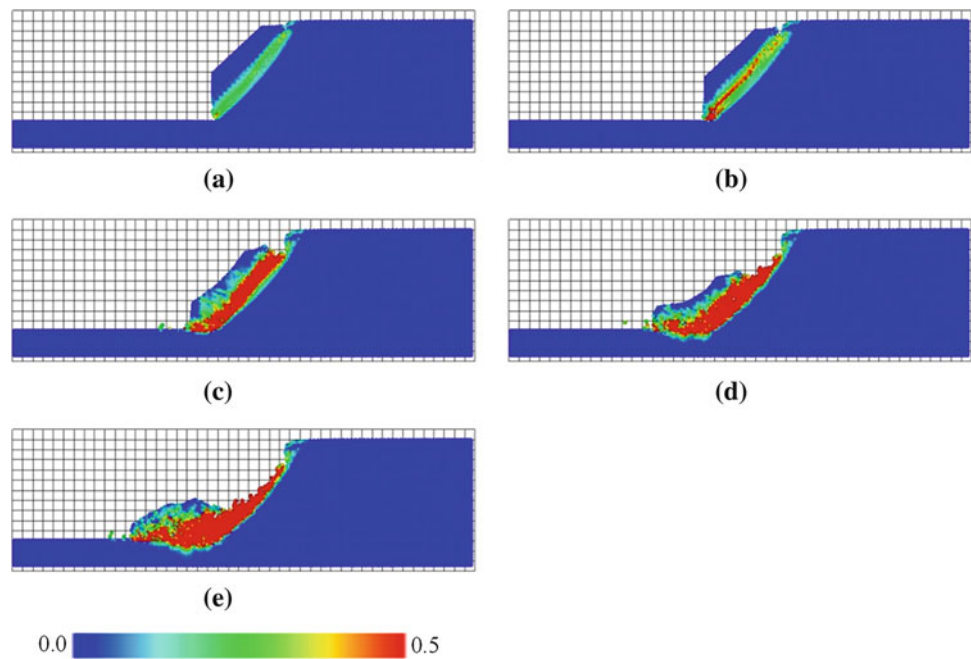


Fig. 26 Distribution of maximum shear strain at an excavation depth of 2.5 m.
a After 1.0 s, **b** After 2.0 s,
c After 3.0 s, **d** After 4.0 s,
e After 5.0 s



vertical direction is free. The bottom boundary of the natural ground is fixed in both directions. The effect of pore water pressure is not taken into account.

Figures 25 show the distribution of the maximum shear strain at each excavation height obtained by SPH. Figure 25 indicates that the modeled embankment deforms when the excavation height reaches 2.0 m, and a massive failure occurred when the excavation depth reached 2.5 m. Deformations of the embankment at different times after the 2.5 m excavation are shown in Fig. 26. Vertical displacements obtained from the experiment, FEM analysis and SPH are

shown in Fig. 27 all together. The values of the safety factor described in the figure are calculated using conventional limit equilibrium method (Fellenius method). Because there is a different between range of displacements obtained by SPH and that obtained in the experiment and FEM analysis, two axes are used in the figure. As we can see from the figure, deformation obtained by FEM is in good agreement with the experimental results before failure, but FEM cannot reproduce large deformation after massive failure. On the other hand, in the result of SPH, although excavation stage of massive failure is little faster than that of the experiment,

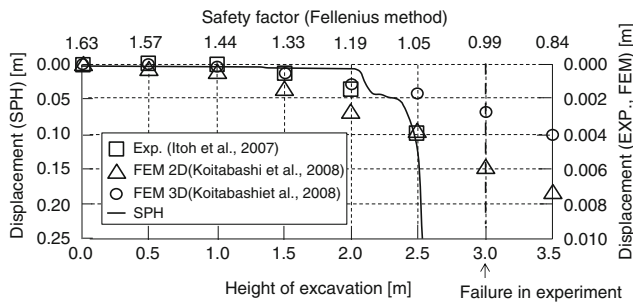


Fig. 27 Distribution of maximum shear strain at an excavation depth of 2.5 m

failure process is roughly reproduced. In addition, it can be seen large deformation after failure is described.

4.4 Sammy of SPH

Based on the comparison between the experimental result and SPH, it is found the SPH has the difficulty in analyzing the stress, strain and deformation in the slope with a high degree of accuracy. This point is a disadvantage of SPH. However, SPH can predict total process, such as small deformation, failure and final flow. Therefore the method is capable of wide application.

5 Concluding Remarks

FEM, CFD, DEM and SPH were introduced as numerical methods for large deformation problems induced by coastal geodisasters. Each numerical method has an advantage for a specific problem. On the other hand, same method has disadvantage for other specific problems. It is still difficult to solve all deformation process, from initial small deformation to large deformation, with high calculation accuracy. It is therefore important for engineers to select an appropriate numerical method for each deformation level based on engineering judgment.

References

- Armstrong, P. J., & Frederick C. O. (1966). *A mathematical representation of the multiaxial Bauschinger effect*, C.E.G.B. Report RD/B/N731. Berkeley Nuclear Laboratories, Berkeley, UK.
- Biot, M. A. (1962). Mechanics of deformation and acoustic propagation in porous media. *Journal of Applied physics*, 33, 1482–1492.
- Borja, R. I. (2006). On the mechanical energy and effective stress in saturated and unsaturated porous continua. *International Journal of Solids and Structures*, 43(6), 1764–1786.
- Cudall, P. A., & Strack, O. D. L. (1979). A discrete numerical model for granular assemblies. *Geotechnique*, 29(1), 47–65.
- de Boer, R. (2000). Contemporary progress in porous media theory. *Applied Mechanics Reviews*, 53(12), 323–369.
- Denlinger, R. P., & Iverson, R. M. (2001). Flow of variably fluidized granular masses across three-dimensional terrain. *Journal of Geophysical Research*, 106(B1), 553–566.
- Fukumoto, S., Unno, T., Sento, N., Uzuoka, R., & Kazama, M. (2007). Estimation of strong ground motions at tsukidate landslide site during the 2003 Sanriku-Minami earthquake. *Journal of Japan Association of Earthquake Engineering*, 7(2), 160–179.
- Gingold, R. A., & Monaghan, J. J. (1977). Smoothed particle hydrodynamics: theory and application to non-spherical stars. *Monthly Notices of the Royal Astronomical Society*, 181, 375–389.
- Gallipoli, D., Gens, A., Sharma, R., & Vaunat, J. (2003). An elastoplastic model for unsaturated soil incorporating the effects of suction and degree of saturation on mechanical behaviour. *Geotechnique*, 53(1), 123–135.
- Itoh, K., Takeyama, M., Toyosawa, Y., & Sano, T. (2007). The development of slope failure detection as a two-dimensional displacement sensor system using a large beam and optical sensor. *Journal of JSCE, Division C*, 63(2), 502–515.
- Itoh, K., & Toyosawa, Y. (2009). Field test of slope failure during slope cutting work. *Journal of JSCE, Division C*, 65(1), 254–265.
- Kazama, M., Takamura, H., Unno, T., Sento, N., & Uzuoka, R. (2006). Liquefaction mechanism of unsaturated volcanic sandy soils. *Journal of Geotechnical Engineering, Japan Society of Civil Engineers*, 62(2), 546–561.
- Koitaabashi, T., Suemasa, N., Itoh, K., & Toyosawa, Y. (2008). Mechanism of slope failure caused by toe excavating. *The 43th Japan National Conference on Geotechnical Engineering* pp. 869–870.
- Koyanagi, K. (2003). Some challenges in earthquake damage surveys. *The Japanese Geotechnical Society*, 52(1), 16–18.
- Lucy, L. B. (1977). A numerical approach to the testing of the fission hypothesis. *Astronomical Journal*, 82, 1023–1024.
- Mori, T., Uzuoka, R., Chiba, T., Kamiya, K., & Kazama, M. (2011). Numerical prediction of seepage and seismic behavior of unsaturated fill slope. *Soils and Foundations* (in press).
- Moriguchi, S., Borja, R. I., Yashima, A., Sawada, K., & Oda K. (2010). Discrete and continuum modeling of sand flow experiment. *Geomechanics and Geotechnics: From Micro to Macro*, pp. 531–536.
- Moriguchi, S., Yashima, A., Sawada, K., Uzuoka, R., & Ito, M. (2005). Numerical simulation of flow failure of Geomaterials based on fluid dynamics. *Soils and Foundations*, 45, 155–166.
- Moriguchi, S., Borja, R. I., Yashima, A., & Sawada, K. (2009). Estimating the impact force generated by granular flow on a rigid obstruction. *Acta Geotechnica*, 4(1), 57–71.
- Sawada, K., Moriguchi, S., Yashima, A., Zhang, F., & Uzuoka, R. (2004). Large deformation analysis in Geomechanics using CIP method. *JSME International Journal, Fluids and Thermal Engineering, Special Issue on CIP, Series B*, 47(4), 735–743.
- Schrefler, B. A. (2002). Mechanics and thermodynamics of saturated/unsaturated porous materials and quantitative solutions. *Applied Mechanics Reviews*, 55(4), 351–388.
- The Japanese Geotechnical Society (2003). Report of Seismic Hazard of Sanriku-Minami Earthquake and Miyagi Prefecture North Earthquake.
- Uzuoka, R., & Borja, R. I. (2011). Dynamics of unsaturated poroelastic solids at finite strain. *International Journal for Numerical and Analytical Methods in Geomechanics*, DOI: 0.1002/nag.1061. (in press).
- Uzuoka, R., Sento, N., Kazama, M., & Unno, T. (2005). Landslides during the earthquake on May 26 and July 26, 2003 in Miyagi. *Japan, Soils and Foundations*, 45(4), 149–163.
- Xiao, F., Honma, Y., & Kono, T. (2005). A simple algebraic interface capturing scheme using hyperbolic tangent function. *International Journal for Numerical Methods in Fluids*, 48, 1023–1040.
- Yabe, T., & Aoki, T. (1995). An universal solver for hyperbolic equations by cubic polynomial interpolation. *Computer Physics Communications*, 66, 219–232.
- Zienkiewicz, O. C., & Shiomi, T. (1984). Dynamic behavior of saturated porous media: The generalized Biot formulation and its numerical solution. *International Journal for Numerical and Analytical Method in Geomechanics*, 8, 71–96.

New Frontiers in Engineering Geology and the
Environment

Proceedings of the International Symposium on Coastal
Engineering Geology, ISCEG-Shanghai 2012

Huang, Y.; Wu, F.; Shi, Z.; Ye, B. (Eds.)

2013, XI, 304 p. 282 illus., 140 illus. in color., Hardcover
ISBN: 978-3-642-31670-8